Genesis of Easterly Waves over the Tropical Eastern Pacific and the Intra-Americas Sea

Victor M. Torres, Chris D. Thorncroft, Nicholas M. J. Hall

Genesis of Easterly Waves over the Tropical Eastern Pacific and the Intra-Americas Sea

VICTOR M. TORRES,[a] CHRIS D. THORNCROFT,[a] AND NICHOLAS M. J. HALL[b]

[a] *Department of Earth and Atmospheric Sciences, University at Albany, State University of New York, Albany, New York*
[b] *University of Toulouse, LEGOS/OMP, Toulouse, France*

(Manuscript received 22 December 2020, in final form 27 July 2021)

ABSTRACT: This paper explores a new mechanism for in situ genesis of easterly waves (EWs) over the tropical eastern Pacific Ocean (EPAC). Using an idealized primitive equation model, it is shown that EWs can be triggered by finite-amplitude transient heating close to the midlevel jet at about 15°N over the EPAC and intra-Americas sea region. The atmospheric response to heating initiates EWs downstream, showing an EW structure within 4 days, with a wavelength and propagation speed of about 2000 km and 4.6 m s^{-1}, respectively, resembling EWs described in the literature. The most sensitive location for EW initiation from finite-amplitude transient heating is located over the northern part of South America and extends to the EPAC. The closer the heating is to the jet, the bigger the response is. A stratiform heating profile is the most efficient at triggering EPAC EWs. Comparisons of simulated EWs over the EPAC and West Africa reveal similar structures but with a shorter wavelength and much weaker amplitudes over the EPAC. EPAC EWs are dominated by horizontal tilts against the shear on the equatorial side of the jet, consistent with barotropic growth, with weaker low-level amplitudes relative to those seen over West Africa. These differences arise from differences in the mean state EPAC having a shorter and weaker midlevel jet with less baroclinicity.

KEYWORDS: Atmosphere; Pacific Ocean; Tropics; Waves, atmospheric; Convection

1. Introduction

Easterly waves (EWs) are westward-propagating disturbances found in the summer season over the tropical band of 15°–20°N across the world. They are observed over West Africa and the Atlantic Ocean (e.g., Kiladis et al. 2006, and references therein), Australia (e.g., Dickinson and Molinari 2000), the western Pacific Ocean (e.g., Serra et al. 2008, and references therein), and the tropical eastern Pacific (e.g., Molinari et al. 1997; Serra et al. 2008; Rydbeck and Maloney 2014, 2015). The characteristics of EWs over the tropical eastern Pacific Ocean (EPAC) and the intra-Americas sea (IAS) have been documented in several studies (Tai and Ogura 1987; Serra and Houze 2002; Petersen et al. 2003; Kerns et al. 2008; Serra et al. 2008, 2010), finding that, on average, they are characterized by meridional wind anomalies of 0.7 m s^{-1}, a phase speed of 5–11 m s^{-1}, a period of 3–5 days, and a wavelength of around 2200 km. Although these general characteristics of EWs over the EPAC have been well recognized, we still lack knowledge and understanding about their life cycle including their genesis and evolution within the complicated mean state found over the EPAC. This paper is concerned with improving our knowledge and understanding of the origin of EWs over the EPAC, motivated by recent studies of genesis over Africa [as in Thorncroft et al. (2008)].

A general consensus exists about the genesis mechanism for EWs over Africa, which is often viewed to be associated with an expression of a linear mixed barotropic–baroclinic instability mechanism (e.g., Burpee 1972, 1974; Norquist et al. 1977; Reed et al. 1977; Thorncroft and Hoskins 1994). Hall et al. (2006) questioned this view highlighting that the African easterly jet was in fact stable to linear growth of African easterly waves (AEWs) in an idealized model when realistic low-level damping was included in a model. Thorncroft et al. (2008) subsequently showed that EWs over Africa could be triggered in a similar setup by localized transient forcing in association with latent heat release close to the entrance of a stable African easterly jet. The EWs that developed in response to the transient heating exhibited structures similar to observed EWs over Africa, suggesting that finite-amplitude triggering was a viable mechanism for EW genesis there. Given this result, it is of general interest to know if it could also explain EW genesis in other regions including the EPAC.

Several mechanisms have previously been proposed to explain the presence of EWs in the EPAC–IAS region. The simplest mechanism is that the EWs propagate into the region from upstream (cf. Frank 1972). Other mechanisms previously proposed include barotropic instability of the mean flow within the region (Mozer and Zehnder 1996; Molinari et al. 1997; Molinari and Vollaro 2000; Maloney and Hartmann 2000), inertial instabilities from cross-equatorial pressure gradients (Toma and Webster 2010b,a), and intertropical convergence zone (ITCZ) breakdown (Ferreira and Schubert 1997). Recently, Rydbeck et al. (2017) suggested another mechanism for the in situ generation of EWs over the EPAC. This consists primarily of the forcing of EWs by local convective disturbances resulting from the high terrain over the northern mountain ranges of South America, next to the Panama Bight. Specifically, they showed in a numerical model simulation, that when the mountains were removed, convection was reduced in the region, as well as downstream EW activity. Whitaker and Maloney (2020) investigated this mechanism with a case study of an EW in June 2012, exemplifying the transition of a mesoscale convective system transitioning into an EW.

Corresponding author: Victor M. Torres, vtorrespuente@albany.edu

DOI: 10.1175/JAS-D-20-0389.1

The triggering hypothesis of AEWs by latent heating was tested via a modeling approach (Thorncroft et al. 2008). This approach consists of two steps: the first one sets up a dry mean state, and the second provides a localized transient heating region to simulate the impact of convection. The results of these experiments showed that the simulated response, after several days of integration, resembled the observed structures of AEWs. Motivated by this, we propose here that EWs over the EPAC can be triggered by a localized convective forcing associated with associated latent heating close to or along the midlevel jet over the EPAC. To achieve this objective, we perform a modeling study, similar to Thorncroft et al. (2008), considering different heating profiles that are representative of the different convective populations over the EPAC–IAS region (Huaman and Schumacher 2018; Zuluaga and Houze 2015).

This paper is organized as follows: Section 2 provides background on the main features of the mean state over the EPAC–IAS. In section 3, we present the data, model, and approach used in this study. Section 4 provides an analysis of the simulated EWs over the EPAC–IAS region in response to a heating trigger based on a stratiform convective profile, considered as a reference. After this, section 5 presents a sensitivity analysis to the heating profile and genesis location. Then a comparison of simulated EWs over the EPAC and West Africa is presented in section 6, to assess similarities and differences between these on different environments. This is followed by a summary and some discussion on the significance of the present findings in section 7.

2. Background: Main features over the EPAC–IAS region

The EPAC–IAS region is characterized by a complex atmospheric mean state in a region of significant variations in topography. To explore how the mean state supports EWs, as well as possible locations for convective triggering over this region, this section presents an overview of the atmospheric state during the extended summer season [June–September (JJAS)] from 1980 to 2015 using data from ERA-Interim (ERAI; Dee et al. 2011). The key atmospheric features are presented in Fig. 1. The wind distribution at 600 hPa in Fig. 1a shows two easterly jet flows: one over the southwestern Caribbean Sea and into the EPAC, and a second one around 2°N, downstream of southern Colombia. In this work we will be focusing on the Caribbean–EPAC jet and it will be referred as ''the midlevel jet'' going forward. In the EPAC the midlevel jet is characterized by a southeast to northwest tilt, clearly departing from a zonal orientation, with peak magnitudes around 6–7 $m\,s^{-1}$. This flow is important for the evolution of EWs, given that most of the atmospheric perturbations [including tropical cyclones (TCs)] track close to the cyclonic shear side of this jet (Kerns et al. 2008; Serra et al. 2010; Brammer and Thorncroft 2015). At 925 hPa (see contours in Fig. 1a), the Caribbean low-level jet (CLLJ) is characterized by easterlies exceeding 12 $m\,s^{-1}$ around 13°N, 73°W, north of Colombia (Amador 1998; Amador et al. 2010; Cook and Vizy 2010). The CLLJ is a dominant local climatic feature over the IAS region that is present throughout the year and characterized by two annual maxima in July and February, with minima in April and October. The CLLJ also extends to about 95°W at its westernmost location through Central America as an intermittent flow, also known as Papagayo jet (Chelton et al. 2000; Romero-Centeno et al. 2007). Previous research suggests that the CLLJ can support localized EW growth through a barotropic growth mechanism (Molinari et al. 1997, 2000; Serra et al. 2010). The focus here, however, is on role of the midlevel jet on EW development.

The vertical structure of the midlevel jet over the EPAC is shown in Fig. 1b. We will focus here on the main region of EW development that occurs between 80° and 100°W and centered at around 10°N on the cyclonic shear side of the jet (see Figs. 3a,b in Serra et al. 2010). We note that the midlevel jet (over the northern side of the EPAC) is located around 15°N and centered at 600 hPa. At low levels, a weak signal is located about 13°N, suggesting a weak contribution from the CLLJ. Over this same region, the distribution of potential temperature θ (in contours) below the jet shows warmer air to the north and cooler air to the south, consistent with thermal wind balance. This low-level temperature gradient, albeit weak, combined with the negative meridional potential vorticity (PV) gradient (discussed below) suggests a possible role for baroclinic growth along the jet.

The dynamic instability of the midlevel easterly jet over the EPAC–IAS region is assessed from a PV perspective, consistent with previous analyses of other tropical easterly jets (Burpee 1972; Thorncroft and Hoskins 1994; Molinari et al. 1997). At 600 hPa, Fig. 1c shows the mean JJAS horizontal distribution of PV. Over the EPAC, relatively high PV is present south of 20°N mostly over oceanic regions (associated with latent heat from convection), while low PV is observed over the Sierra Madre (linked to low stability and elevated dry convection, in a process similar to northern Africa). This distribution of PV results in a local negative meridional gradient in PV roughly parallel to the continent (hatched in Fig. 1c). This distribution then satisfies the Charney–Stern condition for instability of internal jets (Charney and Stern 1962), as well as the Fjortoft condition (Fjortoft 1950), which requires that the mean zonal easterlies are positively correlated with the negative meridional PV gradient (cf. Figs. 1a,c). The fulfillment of these conditions satisfies the necessary conditions for barotropic growth of EWs over this region.

The mean JJAS outgoing longwave radiation (OLR) and rainfall, as retrieved from the Tropical Rainfall Measuring Mission (TRMM) 3B42 product (Huffman et al. 2007), in Fig. 1d, highlight the most convectively active and rainy regions that might provide potential triggering locations for EWs. Notably, the most intense convective and rainy region is over the Panama Bight, located equatorward of the midlevel jet over the EPAC. Previous studies have shown that the associated latent heating found in this region (e.g., Zuluaga and Houze 2015), is collocated with areas of EW genesis (Serra et al. 2010; Belanger et al. 2016; Rydbeck et al. 2017). Convection and rainfall are also generally high over the ocean, west of the continent and over the land regions. In contrast, these quantities are weak over the IAS region, particularly

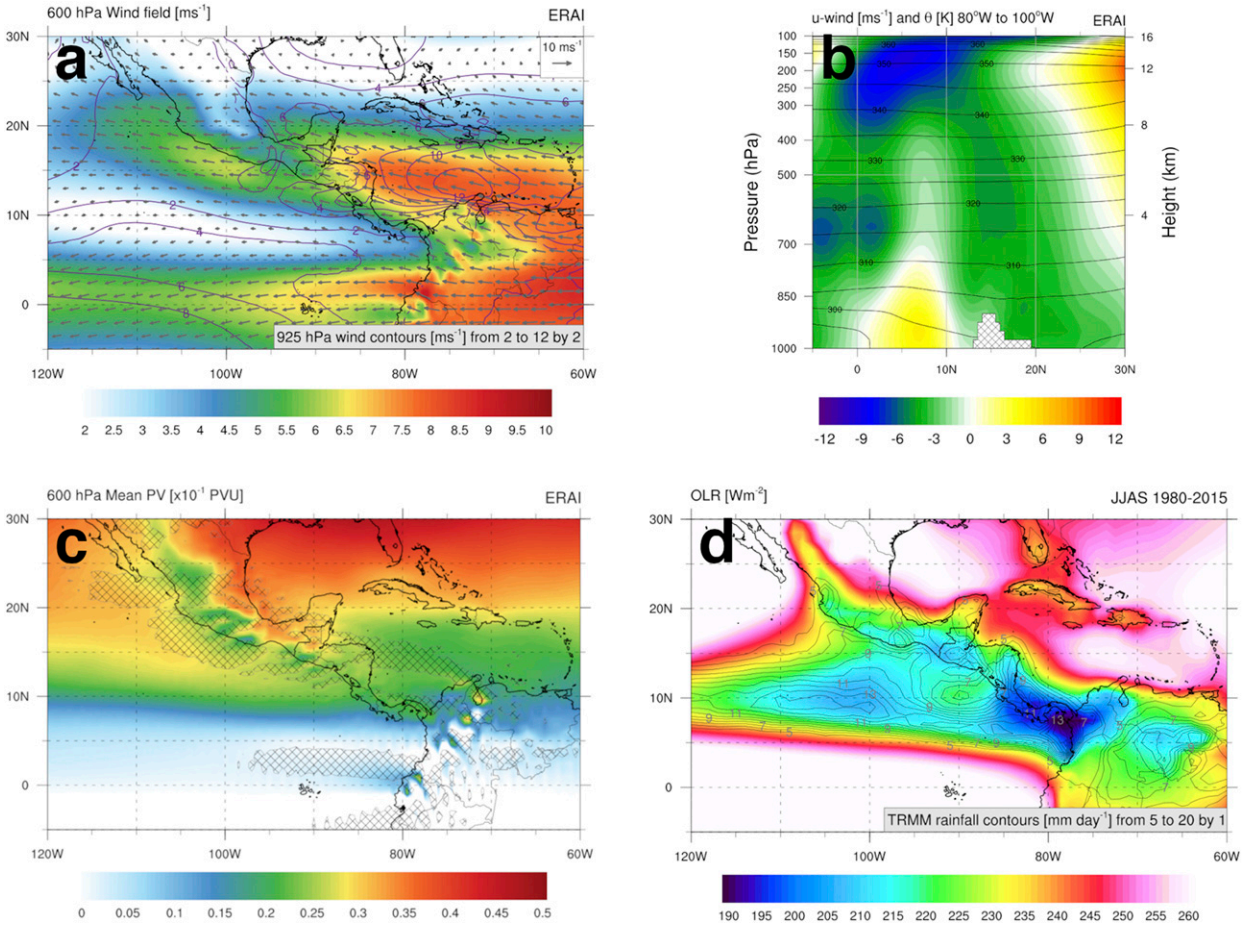

FIG. 1. Climatology of the mean state over the EPAC–IAS region: Wind field (a) magnitude (shading; m s^{-1}) and direction (arrows) at 600 hPa, along with 925-hPa wind magnitude (contours; m s^{-1}). The wind vector scale is indicated for reference. (b) Vertical cross section of zonal wind (shading; m s^{-1}) and potential temperature θ (contours; K) averaged between 80° and 100°W. Cross hatching represents topography at 90°W for reference. (c) Potential vorticity (10^{-1} PVU; 1 PVU = 10^{-6} K kg^{-1} m^2 s^{-1}) at 600 hPa, with areas of negative meridional PV cross hatched, and (d) OLR (shading; W m^{-2}) and TRMM rainfall (contours; mm day^{-1}). The mean is calculated for JJAS during 1980–2015 (for TRMM, only for 1998–2015). The data source is the ERAI at 0.5° resolution for (a)–(c), and NOAA and NASA TRMM for (d).

around 15°N. This is coincident with the location of the CLLJ and cold sea surface temperatures (SSTs) associated with the oceanic upwelling in response to the surface wind stress curl present over the Caribbean, as indicated by Gordon (1967).

In summary, the atmospheric mean state over the EPAC during JJAS is characterized by a southeast to northwest oriented midlevel jet that peaks around 600 hPa. This midlevel flow satisfies the Charney–Stern as well as the Fjortoft necessary conditions for barotropic instability of atmospheric flow and it is consistent with presence of EWs in the region, with a possible role for baroclinic growth along the jet. The OLR and rainfall distributions over the EPAC–IAS region suggest that triggering of EWs via latent heating could most likely occur over the Panama Bight region, equatorward of the midlevel jet. We hypothesize that these features together, set up a suitable environment for triggering of EWs over the EPAC. Having identified the main features or the mean state over the EPAC, we provide in the next section the characteristics of the model used, as well as an assessment of how well the features here introduced are captured by this model given its resolution.

3. Data and modeling approach

The overall approach used in this research follows that in Thorncroft et al. (2008). This consists of exploring the dry adiabatic response to finite-amplitude, transient heating perturbations, to assess the extent to which such perturbations are able to trigger EWs in the EPAC region. The characteristics of the model used for these simulations are described next.

a. Model

The model and setup used for this research is described in Hall et al. (2019), which is an improved version of the model used in Thorncroft et al. (2008). This is a dry, global, spectral primitive equation model, with truncation at wavenumber

number 42 (T42), corresponding to a horizontal grid of about 2.8° at the equator, and 15 vertical levels (L15), close to ERAI standard levels, in a sigma (σ) coordinate system. A 12-h–∇^6 horizontal diffusion is applied to the momentum and temperature equations. However, differences with the previous version include a linear vertical diffusion scheme, instead of a simple in situ damping. This is applied to momentum and temperature equations on time scales of 16 h below $\sigma = 0.80$ and of 20 days above this. Also, there is additional regional drag on momentum, which is doubled over land at the lowest level. In addition, a separate vertically uniform damping is also applied on temperature, with a time scale of 12 days, as a simple representation for longwave radiative cooling. With these damping and diffusion parameters, the global mean atmosphere remains baroclinically unstable in the extratropics in all seasons, and the tropical atmosphere is stable, including the easterly jets, just as it was in Thorncroft et al. (2008). Integrations of the full nonlinear equations for vorticity, divergence, temperature, and surface pressure are carried out with a 22.5-min semi-implicit time step. As in similar studies using this model (Hall 2000; Hall et al. 2006; Thorncroft et al. 2008), the basic state is maintained by adding a forcing term that represents the combined effects of diabatic heating and transients. The model experiments were constrained to be linear by rescaling the perturbations. This model setup will also be used later to perform simulations over Africa, similar to those in Thorncroft et al. (2008).

A basic run involves prescribing the heating in a particular location for a period of one day and then switching it off. The model is integrated for several days after this to see the adiabatic response to this transient heating. After the first day, no heating is included within the developing EW, and so it is expected that EW amplitudes will be weaker than those observed or seen in models with full physics (e.g., Serra et al. 2008, 2010; Crosbie and Serra 2014; Rydbeck and Maloney 2014, 2015). The main objective of this work is to identify whether upstream heating can lead to realistic EWs downstream and to investigate the impact of the heating on the nature of these EW developments.

b. Data

The data used for this model were obtained from the ERAI reanalysis (Dee et al. 2011) and ingested into the model at T42 horizontal resolution and with 15 vertical levels (see Fig. 2). Figure 2a highlights the presence of the midlevel easterly jet at the $\sigma = 0.600$ level. Easterlies over the EPAC peak around $7\,\mathrm{m\,s^{-1}}$, closely reproducing those values from the full resolution ERAI reanalysis (cf. Fig. 1a). In the vertical, the zonal and meridional winds reproduce nicely these features (cf. Fig. 1b), also evidencing the absence of topography from the model in this vertical average.

The distribution of mean PV at the same level from the model in Fig. 2c shows high PV over oceanic regions and low PV over regions close to continental areas, consistent with that from ERAI reanalysis in Fig. 1c. However, this distribution presents a very weak negative meridional PV gradient over the region, which is expected given the coarser resolution of the model.

c. Heating profiles

The initial localized heating is prescribed in the model through the thermodynamic equation, following Thorncroft et al. (2008). In the horizontal, the heating function is given by the form

$$H(r) = \begin{cases} H_0 \cos^2 \dfrac{\pi}{2}\left(\dfrac{r}{r_0}\right), & |r \le r_0 \\ 0, & |r > r_0 \end{cases},$$

where H_0 is the peak heating rate at the center, r is the distance from the center, and r_0 determines the horizontal scale of the heating. For the basic heating run, r_0 is set to 7.5°. Heating runs with 3° and 5° were performed, showing only differences in amplitude without affecting the general structure (not shown). The heating is centered at 7°N and 78°W (illustrated in Fig. 3a) downstream of the Colombian Andes and over the Panama Bight. This location represents a region of heating associated with enhanced mean convection over the region of the Gulf of Panama (Zipser et al. 2006; Zuluaga and Houze 2015; Huaman and Schumacher 2018), and we hypothesize that the convective forcing there can trigger EWs over the EPAC, as recently investigated by Rydbeck et al. (2017) and Whitaker and Maloney (2020).

All the heating functions used in this work are based on Thorncroft et al. (2008). We initially considered the one characterized by a stratiform heating–cooling profile, with the analytic form given by

$$H_0 = \frac{75\pi}{(71 - 18e^{-2\pi})}[e^{-2\pi(1-\sigma)} - 1]\cos\frac{3\pi}{2}(1-\sigma),$$

illustrated by the gray line in Fig. 3b. This profile was considered first because of the known dominance of stratiform heating–cooling in the Panama Bight (Zuluaga and Houze 2015). According to Hertenstein and Schubert (1991), such a profile is efficient in generating cyclonic PV anomalies (and their associated relative vorticity) in the midtroposphere. This vorticity is caused by strong heating gradients in the vertical at such levels. The peak heating rate for this profile is $3.12\,\mathrm{K\,day^{-1}}$ at $\sigma = 0.312$, and a cooling rate of $-1.47\,\mathrm{K\,day^{-1}}$ at $\sigma = 0.850$. This profile integrates to unity between $\sigma = 0$ and $\sigma = 1$ (as well as the others illustrated; hence they all account for the same total heating to the system). For our purposes the stratiform profile is of particular interest given the emphasis here on EWs at $\sigma = 0.600$ and given the favorable dynamical conditions for EW growth found in the mean state at this level.

Recognizing that the EPAC–IAS region is impacted by different types of convection with different heating rate profiles (Schumacher et al. 2004; Zuluaga and Houze 2015; Huaman and Schumacher 2018), two additional convective profiles were considered: shallow and deep convective. The functional form for the shallow profile is given by

$$H_0 = \left(\frac{1}{\pi} - \frac{12}{\pi^3} + \frac{48}{\pi^5}\right)^{-1} \sigma^4 \sin(\pi\sigma),$$

and that for the deep convective profile is given by

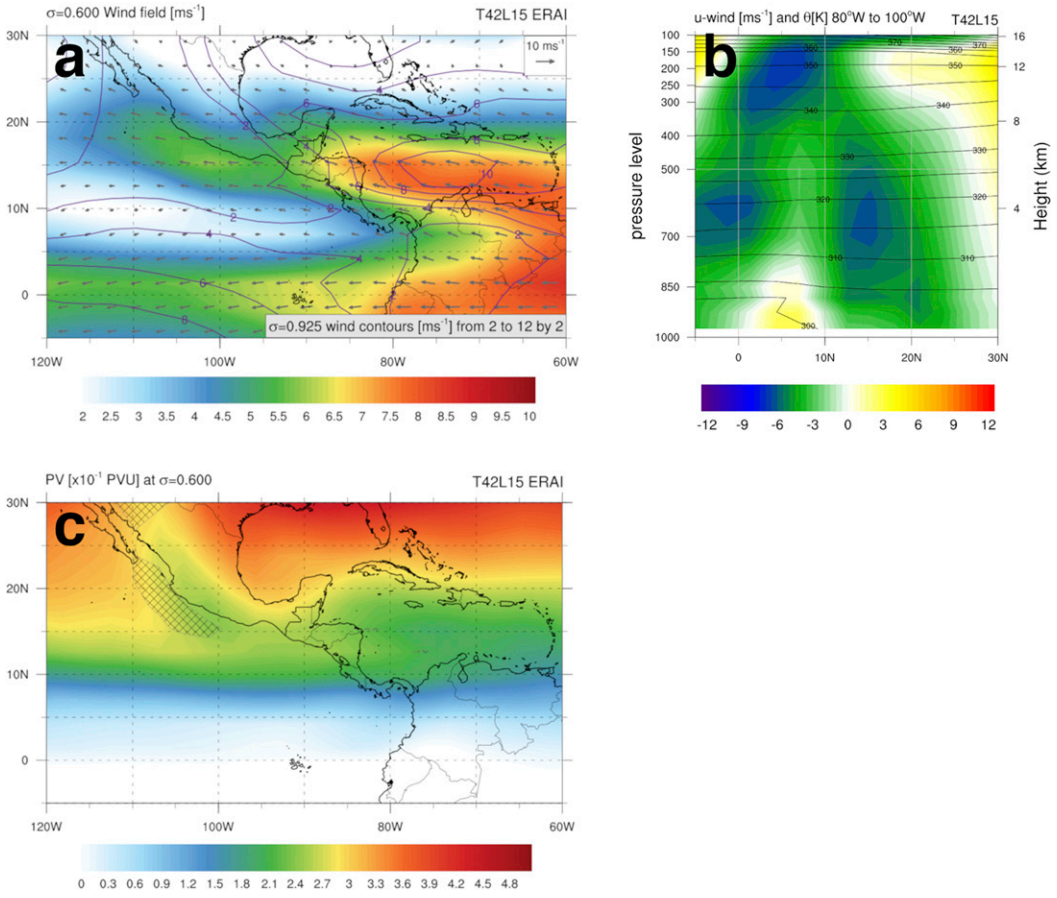

FIG. 2. Main features over the EPAC–IAS region from the T42L15 model: (a) Wind field magnitude (shading; $m\,s^{-1}$) and direction (arrows) at $\sigma = 0.600$ hPa, along with wind magnitude at $\sigma = 0.925$ hPa (contours; $m\,s^{-1}$). The wind vector scale is indicated for reference. (b) Vertical cross section of zonal wind (shading; $m\,s^{-1}$) and potential temperature θ (contours; K) averaged between 80° and 100°W. The vertical coordinate is $\sigma \times 1000$, approximately the same value of pressure in hectopascals. (c) Potential vorticity (10^{-1} PVU) with areas of negative meridional PV cross hatched. The data are ingested from the ERAI reanalysis for JJAS 1980–2015.

$$H_0 = \frac{\pi}{2}\sin(\pi\sigma),$$

both also included in Fig. 3b. Peak heating rates of the shallow and deep convective profiles are 2.71 K day^{-1} at $\sigma = 0.792$ and 2.09 K day^{-1} at $\sigma = 0.500$, respectively.

4. Easterly waves forced by localized stratiform heating

The atmospheric response to stratiform heating is shown in Fig. 4 with relative vorticity at $\sigma = 0.600$. After an initial adjustment to the heating during day 1, the evolution in the relative vorticity field is characterized by a coherent EW wave train downstream of the initial heating location. The initial heating directly spins up a trough at $\sigma = 0.600$ (Fig. 4a) similar to that seen in Thorncroft et al. (2008). A gravity wave is also triggered by the initial heating that propagates quickly away from the region. By day 4, a clear and well-defined EW structure is formed, with troughs and ridges, that resemble observed EW structures over the EPAC (Serra et al. 2008, 2010; Crosbie and Serra 2014; Rydbeck and Maloney 2014, 2015; Rydbeck et al. 2017). It is interesting to note that after day 3, the initiation points for the following ridge and trough, are slightly displaced upstream (to the east). This may be consistent with a weak upstream development signal similar to that seen over West Africa (Diaz and Aiyyer 2013) and should be considered in future work. By day 6 the EW structures are less coherent and appear to be dissipating (Fig. 4f). The initial vortex is also much weaker by this time as it reaches about 105°W just west of southern Mexico.

The simulated EWs track parallel to the coast following the negative PV gradient observed at midlevels, as well as the horizontal winds (see Fig. 2). They propagate northwestward with a phase speed of about 4.6 $m\,s^{-1}$ and are characterized by a wavelength of about 2000 km. Additionally, they present northeast to southwest horizontal tilts south of the jet, consistent with barotropic growth. These structures are similar to those from previous observational studies (Serra et al. 2008, 2010; Rydbeck and Maloney 2014, 2015) with EWs characterized by a northeast–southwest tilted and elongated structure, with positive and negative anomalies of relative vorticity over the EPAC. The amplitudes of the simulated EW vorticity

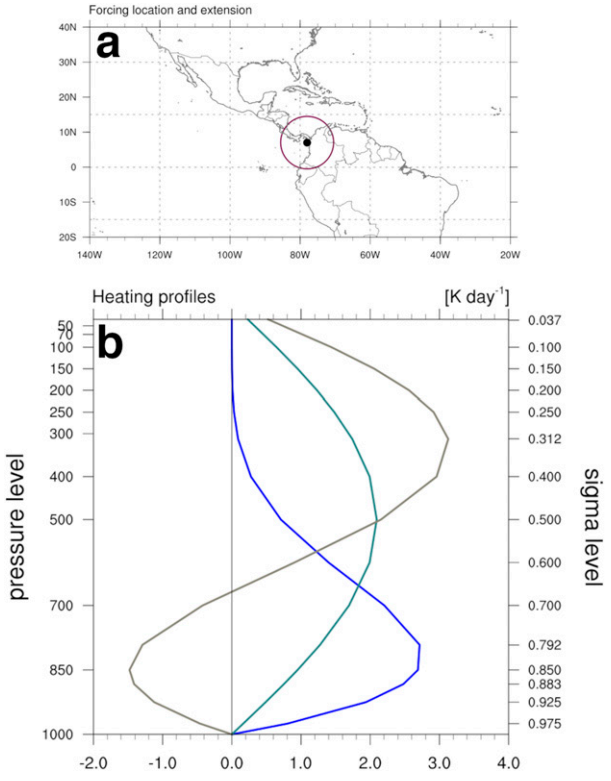

FIG. 3. Triggering location and heating profiles used: (a) Center point (7°N, 78°W) where these heating profiles were used (in black) and radius of the heating (7.5°). (b) Stratiform convective (gray), deep convective (green), and shallow convective (blue) profiles, analogous to Thorncroft et al. (2008). The vertical coordinate on the left exemplifies pressure levels (hPa), which is approximately $\sigma \times 1000$, as noted on the right side. The horizontal axis shows normalized magnitude, with each profile integrating to 1 in the vertical direction.

anomalies are about $4 \times 10^{-6}\,s^{-1}$, which is close to the magnitudes of $3 \times 10^{-6}\,s^{-1}$ from observed EWs in composite studies south of the Isthmus of Tehuantepec (Rydbeck and Maloney 2014, 2015).

To explore the vertical structure of these simulated waves, Fig. 5 shows a vertical cross section of the meridional wind (with vertical levels indicated in hPa, as previously noted) along the purple line included in Fig. 4d. The vertical structure (left column in Fig. 5) during the first day shows a vertical development consistent with the direct response to the stratiform heating profile, characterized by a midlevel trough centered around 600 hPa. There is also a ridge response at lower and upper levels (900 and 150 hPa, respectively) also seen on day 1 in Thorncroft et al. (2008). During the subsequent days, the midlevel trough propagates westward with the peak rising to about 500 hPa. By day 4 (Fig. 5d), the meridional wind shows a maximum between 800 and 250 hPa, reaching values of $1.4\,m\,s^{-1}$. This value is similar to the value obtained in the composite EWs of Serra et al. (2008), who found a value of $0.9\,m\,s^{-1}$. Also, at this time in its evolution (Fig. 5d), the wave has lost most of its lower- and upper-level ridge signals. Throughout the evolution of these EWs, the meridional wind also indicates an eastward tilt with height below the mean jet (highlighted in Fig. 5d), suggesting a role for baroclinic growth of the simulated EWs.

Overall, the results of this simulation provide evidence to support the initial hypothesis that EWs over the EPAC can be forced by a finite-amplitude, transient heating, through a downstream adiabatic response. The next section explores the sensitivity of this downstream response to the heating profile and its location.

5. Sensitivity to heating and location

Based on the different convective populations found over the EPAC–IAS region previously stated, this section provides a sensitivity analysis to convective profiles followed by a sensitivity to the location of heating. All the results will be presented at the level of $\sigma = 0.600$ to explore the atmospheric responses at the level of the midlevel jet.

a. Sensitivity to heating profiles

1) SHALLOW CONVECTIVE HEATING PROFILE

The atmospheric response to transient shallow heating in the horizontal ($\sigma = 0.600$) is shown in Fig. 6, above the level of maximum heating at $\sigma = 0.792$. A midlevel ridge is seen in the relative vorticity field (see Fig. 6a). By day 2, the ridge has moved westward along the jet and a weak upstream trough has also formed, resulting in an EW-like structure. It is weaker than that for the stratiform case and weakens further during the subsequent days, and by day 4, the vorticity field does not present a coherent wave structure (see Fig. 6d).

In the vertical direction (Figs. 5e–h), the response is characterized by a midlevel ridge above a low-level trough by day 1, consistent with peak heating in the lower troposphere (see Fig. 5e). This vertical structure reflects a weaker development at the jet level (in comparison with the stratiform case). This results from the initial wind response to the heating imposed, resulting in different relationship between these winds and the midlevel jet over the EPAC (see Fig. 3 for reference). Examples of the response are observed in the vertical structures on day 1 in Figs. 5a and 5e. Whereas at 600 hPa the shallow convective produces $\sim 1.20\,m\,s^{-1}$, the stratiform profile produces a meridional wind of $\sim 3.20\,m\,s^{-1}$, suggesting a weaker interaction from shallow convection the level of the jet. Last, a tilt in the vertical direction is again present (see Fig. 5h), suggestive of baroclinic growth.

Overall, a shallow heating perturbation results in a weaker EW response along the midlevel jet in comparison with EWs forced by the stratiform heating profile. The perturbation structures resemble weak EWs over the EPAC, but their quick decay suggests that shallow convection is less efficient at triggering EWs. This is likely due to the reduced impact this type of heating has in forcing circulations close to the midlevel jet.

2) DEEP CONVECTIVE HEATING PROFILE

For completeness, a run initialized with a deep convective heating profile was also performed. As in the previous two cases, the results of the perturbation run are shown at the $\sigma =$

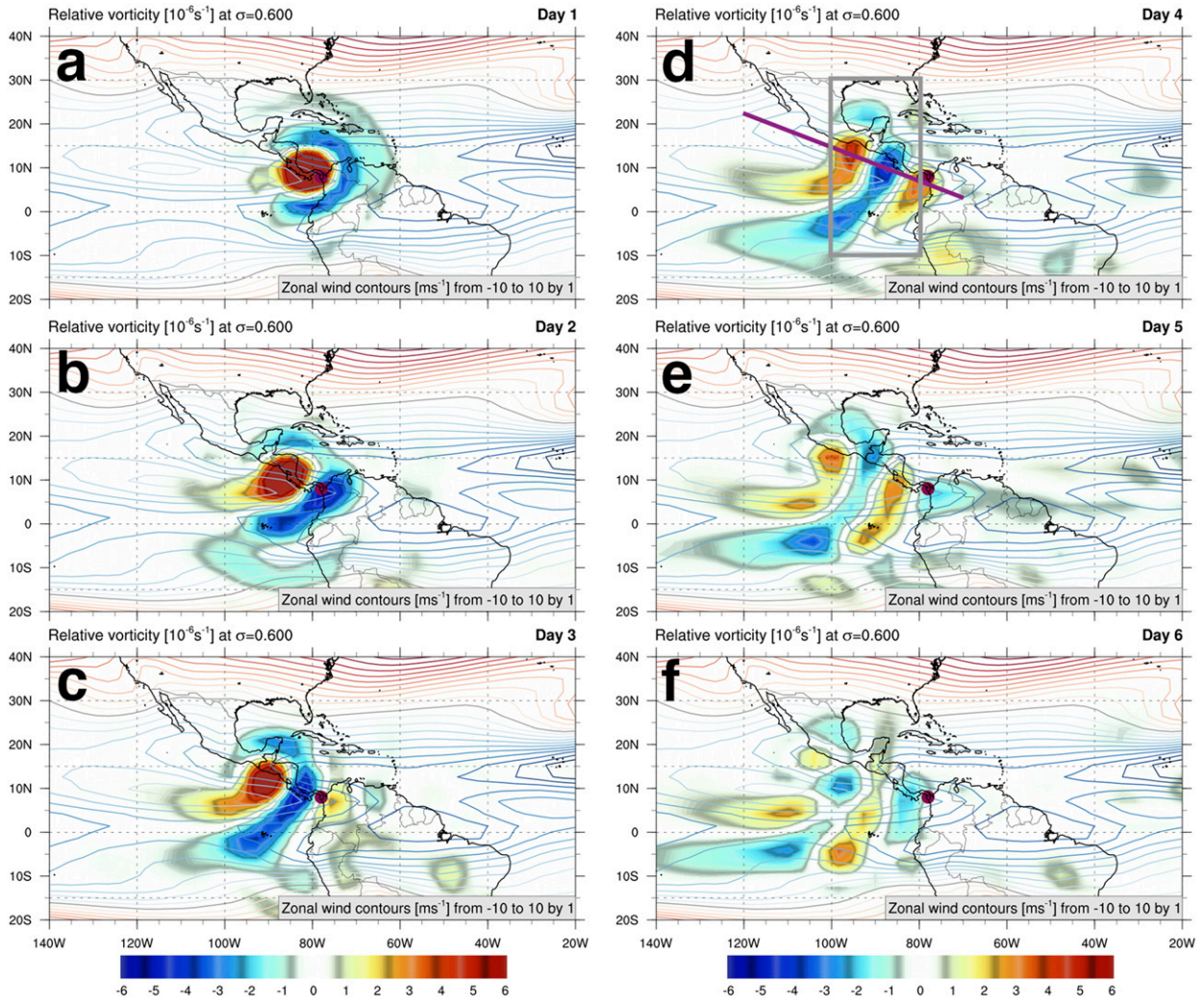

FIG. 4. Relative vorticity (shading; $10^{-6}\,s^{-1}$) at $\sigma = 0.600$ for days 1–6 for the response to a stratiform convective anomaly at 7°N, 78°W. Contours show the zonal wind ($m\,s^{-1}$) at the same level, with red colors referring to westerlies, blue colors referring to easterlies, and the gray contour indicating zero. The purple diagonal line on day 4 is a reference for the vertical cross sections in Fig. 5 below, and the gray-outlined box shows the area used later for averages in Fig. 10.

0.600 level, which in this case is below the level of maximum heating (at $\sigma = 0.500$). The horizontal evolution of relative vorticity in Fig. 7 is very similar to that seen initialized with the stratiform profile, albeit weaker (cf. Fig. 4). This can be further appreciated by day 4 (Fig. 7d) when the system shows a weak and coherent structure quickly decaying as observed by day 6 (Fig. 7f).

The growth of EWs initiated by a deep convective heating profile is weaker at $\sigma = 0.600$ due to the location of the applied latent heating with respect to the midlevel jet. This is seen in the vertical structure of the generated EWs (right column of Fig. 5), where maximum amplitudes in meridional wind are at 700 hPa (below the jet level at about 600 hPa), are weaker in comparison with the stratiform heating profile. The vertical structure is also characterized by a weaker tilt in the vertical (when compared with stratiform and deep convective profiles), which suggests that baroclinic processes may contribute less to the growth of EWs from this convective profile. Additionally, the vertical structure shows a secondary maximum developing between days 2 and 4 at lower levels, between $\sigma = 0.925$ and $\sigma = 0.883$, and evolving to midlevels. This is simply the initial response to the heating profile and the eventual establishment of a midlevel EW taking advantage of midlevel PV gradients.

Overall, the deep heating perturbation result in a similar but weaker EW response along the midlevel jet when compared with the EWs forced by the stratiform heating profile. The deep convection profile generates EWs that persist longer than those generated by the shallow convection heating profile. Once again, this is explained by noting that the deep heating gradients force circulations closer to the level of the midlevel jet.

In summary, model runs with different heating profiles over the EPAC–IAS region show triggering of EWs, but the type of heating profile determines their general structure and

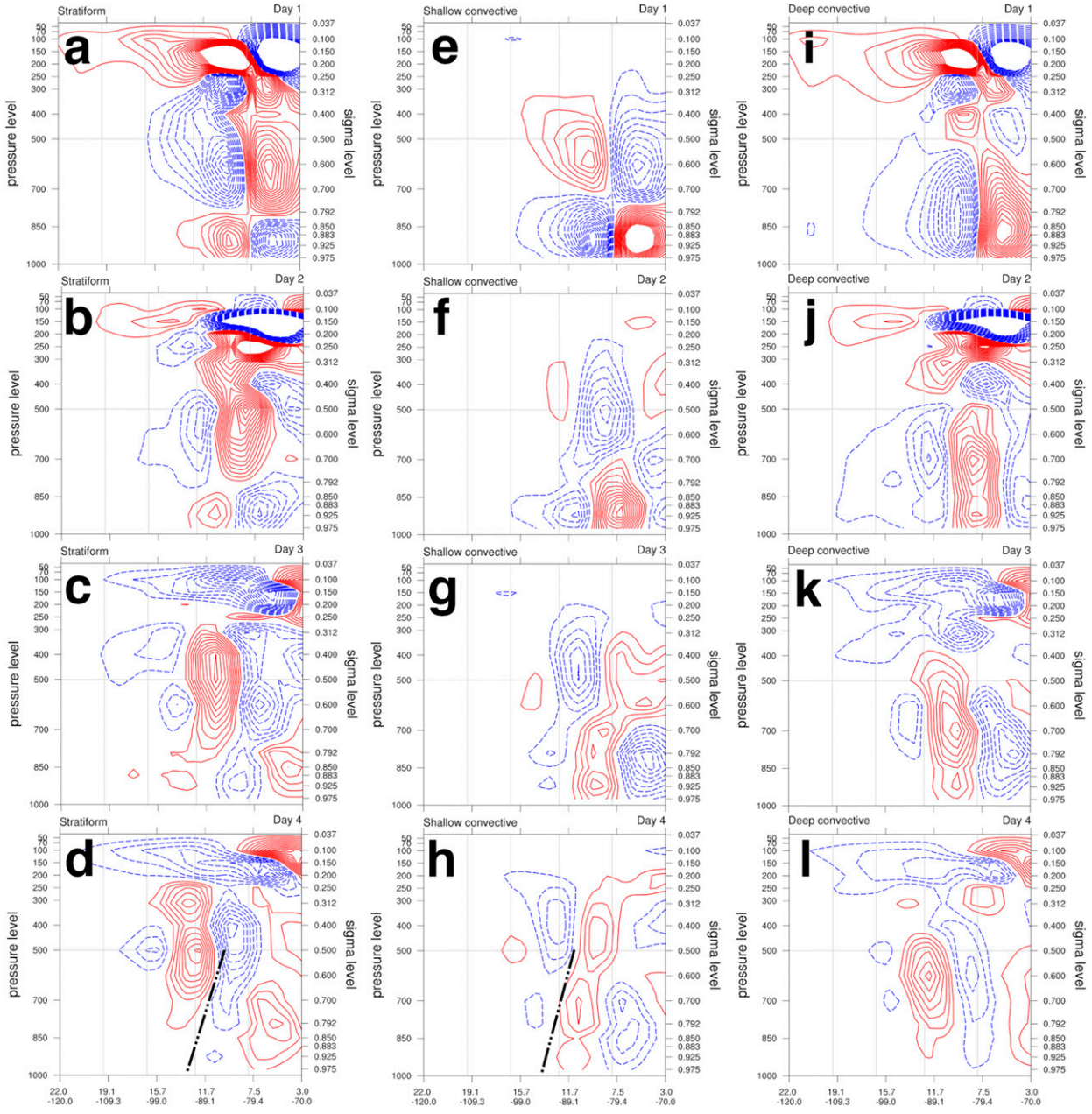

FIG. 5. Vertical cross section of meridional wind ($m\,s^{-1}$) across the line in Fig. 4d for days 1–4 for the three different heating profiles. Contours are every 0.20 $m\,s^{-1}$ for the stratiform and shallow profiles and 0.10 $m\,s^{-1}$ for deep convective, with negative contours dashed in blue. The vertical coordinate is $\sigma \times 1000$, which is approximately the same value of pressure in hectopascals. The dashed line in (d) and (h) is to highlight the vertical tilting.

evolution, indicating sensitivity to the nature of the heating profile. The deep convective heating profile drives an initial midlevel trough close to the jet level. In contrast, the shallow convective profile generates a low-level trough, with a very weak response at the jet level. These three heating profiles all lead to a shared vorticity structure with an upper-level anticyclone above a cyclone. The cooling in the stratiform heating profile results in an additional low-level anticyclone. The results suggest that the closer the vertical heating gradients, and associated PV tendencies are to the level of the jet, the stronger the downstream EW response is along the jet.

b. *Sensitivity to location of heating*

So far, the results have only shown the EWs triggered by heating at one location, centered in the Panama Bight region at 7°N, 78°W. However, convection and its associated heating occurs over a wider region over the tropical EPAC and IAS regions (see Fig. 1d, and also Zuluaga and Houze 2015, their

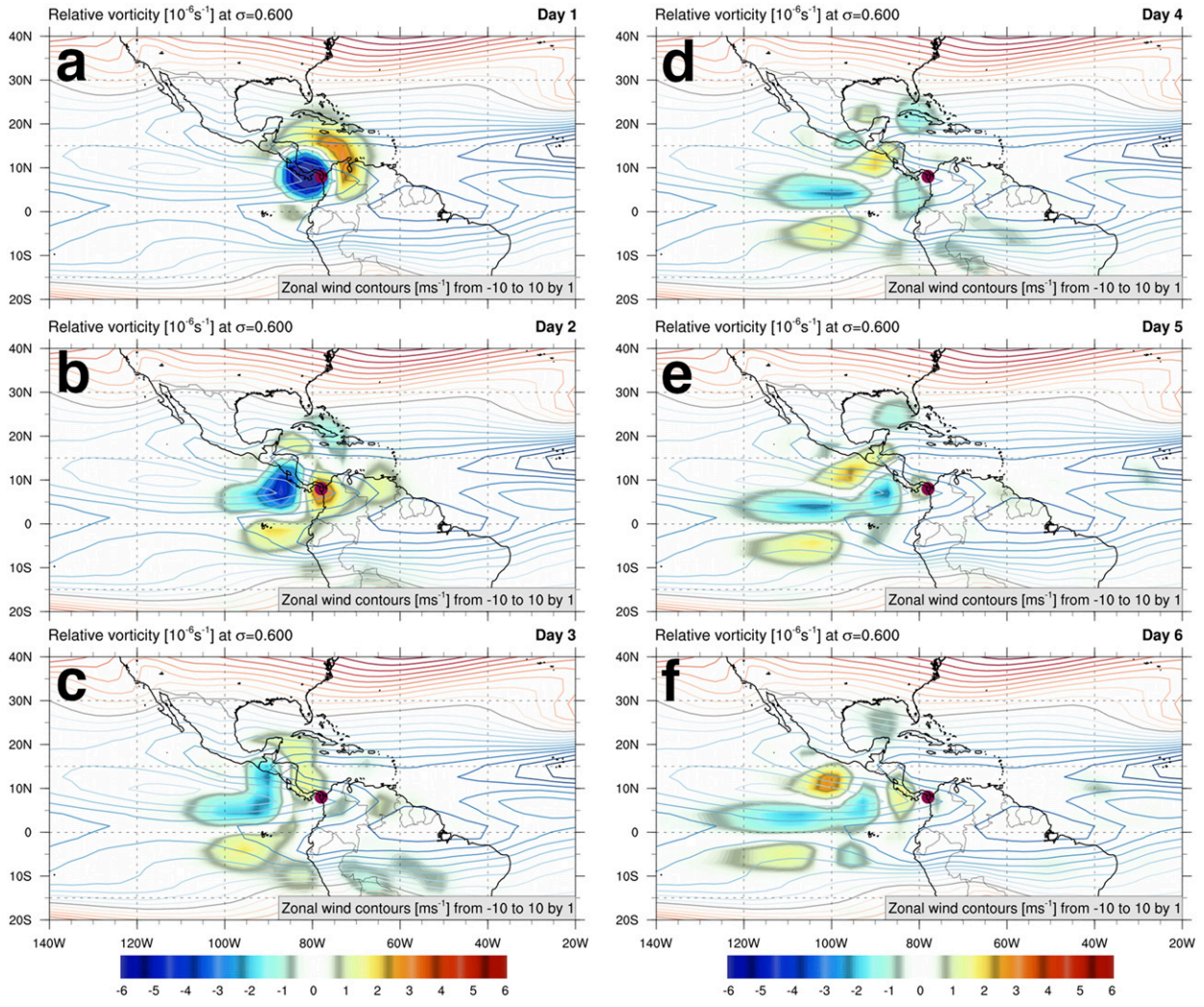

FIG. 6. Relative vorticity at $\sigma = 0.600$ (shading; $10^{-6}\,s^{-1}$) for days 1–6 for the response to a shallow convective anomaly at 7°N, 78°W. The contours show the zonal wind ($m\,s^{-1}$) at the same level, with red colors referring to westerlies, blue colors referring to easterlies, and the gray contour indicating zero.

Fig. 3). Motivated by this, the impact of changing the heating location on the EW response over the EPAC–IAS region was explored. This will help to identify the most efficient location to force EWs over the region for the current basic state. To achieve this, a large number of simulations were performed over the region enclosed between 5°S and 35°N, and between 50° and 120°W with a spacing of about 3° in latitude and longitude. This region is indicated by the green-outlined box in Fig. 8.

The results of these simulations are also shown in Fig. 8 (shading) by using an influence function for the three different profiles. We defined this influence function as the spatial variance of relative vorticity at $\sigma = 0.600$ on day 4 of the simulation over a target area of 0°–20°N and 75°–105°W (shown outlined in red in the same figure).

The stratiform heating profile in Fig. 8a shows a peak region around 12.5°N, 70°W extending from the tropical EPAC trough Central America and into the western Caribbean. This is located along the midlevel jet over the northern region of South America over the Caribbean Sea, ranging in latitude from 5° to 20°N. This suggests that the best (or most efficient) location to force EWs over the EPAC–IAS region is around 12.5°N, 70°W. This region is located northeast of the initial point in the basic runs, which is outside of the strongest influence region. Also, we observe that the influence function is much stronger for the stratiform heating profile (Fig. 8a) when compared with shallow (Fig. 8b) and deep (Fig. 8c) convective profiles. This can be explained by the stronger interaction with the midlevel jet, as previously discussed.

While the focus of our work is on EW activity in the region of the midlevel jet, we also explored the influence functions for responses in the target area (red box) at different levels. While all three heating profiles trigger midlevel EWs in the target area, we also noted that the stratiform and deep heating profiles also trigger a significant response at upper levels, around $\sigma = 0.200$ (not shown). Interestingly, there are two distinct favored regions for triggering this response; one upstream of the midtropospheric easterly jet in the Caribbean–Panama

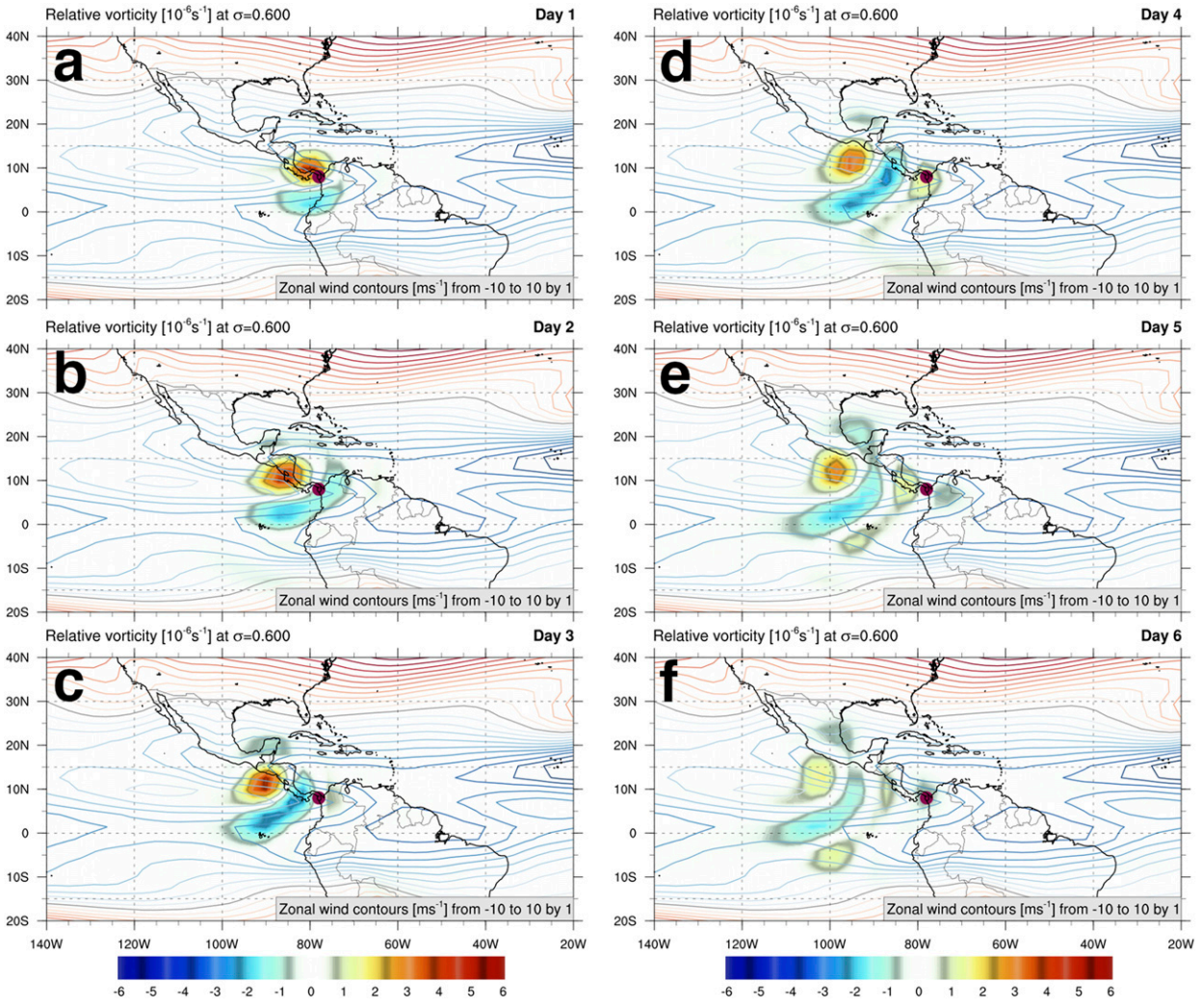

FIG. 7. As in Fig. 6, but for a deep convective anomaly.

Bight region, and a second farther north in the Gulf of Mexico, close to the subtropical westerly jet. Likely, this is linked to the vertical heating gradients associated with the stratiform and deep heating profiles, perturbing the upper-level westerly jet region, and resulting in a Rossby wave response that impacts the target area. While this is beyond the scope of the current work, we recommend that this be explored more in the future.

We also explored the sensitivity of our results to extending the target area farther west to 125°W (based on observations of EW density over the EPAC). Interestingly, the most likely region for genesis of EWs is still in the same spot north of South America. In addition, a secondary maximum was found west of Mexico at about 15°N, 100°W on the cyclonic side of the jet. While weaker in magnitude, this is due to the fact that we are now including EWs farther west outside our main target region. Overall, this extended target region still supports our main result that the most efficient region to force EWs is north South America, close to the midlevel jet entrance.

Overall, these results suggest that the best location to initiate EWs in the EPAC is along the midlevel jet, in the western and central Caribbean. The mean OLR shown in Fig. 1d suggests reduced convective activity in this region, relative to the Panama Bight region, for example. However, the results of Funk et al. (2013), based on the TRMM 2A23 product describing convective types, highlight the presence of convection at this region (particularly stratiform) albeit at a lower frequency. While this is suggestive of the fact that this region may not favor frequent convective triggering of downstream EWs, it should be recognized that other triggering mechanisms might also operate. For example, this could include dynamical triggering linked to dry EWs from the upstream Atlantic (see Serra et al. 2010; Brammer and Thorncroft 2015), midlatitude intrusions, or other tropical waves (Kiladis et al. 2009). These hypotheses, however, also require further research.

We now briefly compare the EW structures resulting from stratiform forcing located at three locations. Figure 9 shows the relative vorticity at day 4 (left column) and, in order to see the

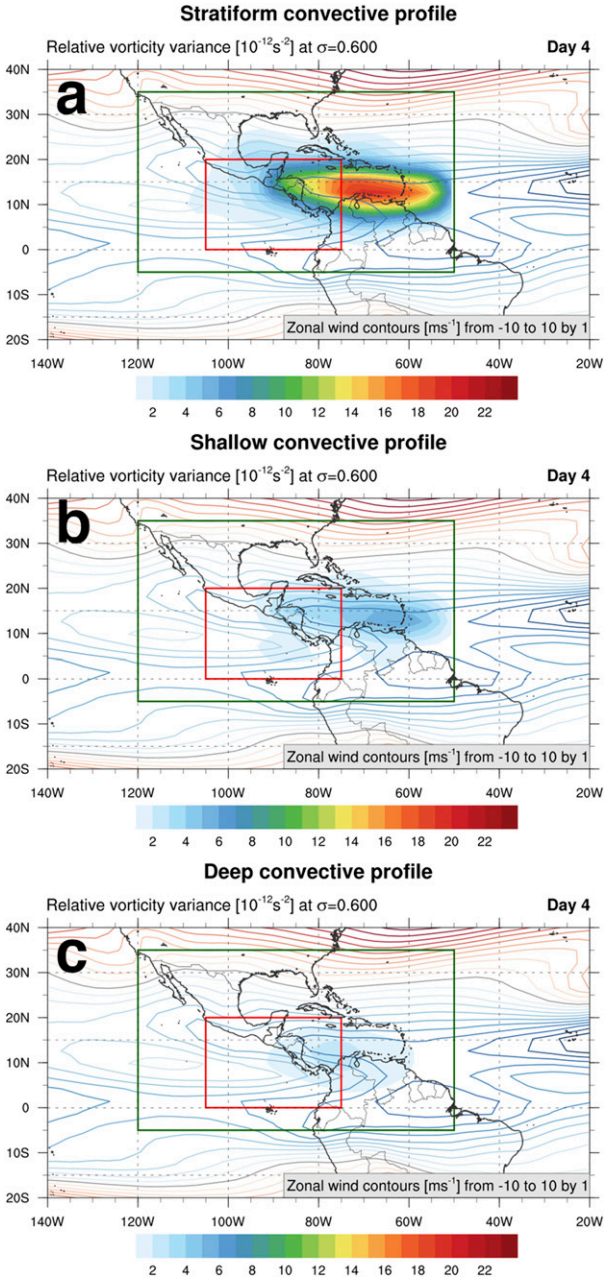

FIG. 8. Influence function for (a) stratiform, (b) shallow, and (c) deep convective anomalies at $\sigma = 0.600$. Shading shows the most sensitive location for the initiation of EWs over the EPAC–IAS region that have high amplitude on day 4 in the red-outlined box. The contours show the zonal wind ($m\,s^{-1}$) at each level, with red colors referring to westerlies and blue colors referring to easterlies. The green-outlined box shows the forced region.

EW structures in the EPAC, we also look at later days (right column). Figure 9a shows the response to heating at the location of most efficient forcing at 12.5°N, 70°W. After four days (Fig. 9a, left), the horizontal structure shows a trough over the Yucatan peninsula with tilted structures oriented against the shear of the midlevel jet associated with barotropic growth over the western Caribbean. On this day, a second trough is initiated over the Panama Bight, forming a well-defined wave train. These characteristics show similarities with the EWs forced by heating at the reference location at 7°N, 78°W in Fig. 4. By day 6 (Fig. 9a, right) the leading vorticity maximum is located over Mexico maintaining a somewhat circular structure. The following trough is characterized by a double peak structure with maxima over the east Atlantic and the Gulf of Mexico, as retrieved from regressions (Serra et al. 2010) and observed during Hurricane Ingrid over the Atlantic and Hurricane Manuel over the EPAC in 2013, where upper-level circulations have demonstrated that both storms cannot be considered isolated (Allison et al. 2018). This structure is similar, though weaker, at day 8 from this forcing location (not shown).

Figure 9b shows the response to heating at 10°N, 55°W located over the Atlantic Ocean at day 4. This point was selected because of a maximum in the tropical depression (TD) band. To recall, the TD band (Takayabu and Nitta 1993) is defined as westward-moving fluctuations with period of 2–10 days and wavenumber 6–20, which includes EWs. This location is also useful to observe the evolution of heating associated with upstream AEWs moving in from the Atlantic. The forced response moves westward, and the initial trough has maintained its initial circular structure, directly forced by the initial heating. The following ridge and trough form a tilted structure against the shear of the midlevel jet over the Caribbean Sea by day 4. By day 8 (Fig. 9b, right), the leading trough is over the continent with a structure similar to that obtained with forcing over the tropical EPAC on day 4 (Fig. 4d). Heating over the Atlantic suggests that upstream heating located along the axis of the midlevel jet induce EWs over the EPAC–IAS region.

Last, a location south of the midlevel jet at 0°N, 78°W (Fig. 9c, left) was considered to study the effects of a localized forcing far from the jet region where the dynamical conditions for their growth (through barotropic instability) are not met. This figure shows that there is not a clear EW development forced from this point, with an atmospheric response quickly decaying by day 4. By day 6, all the relative vorticity anomalies have already dispersed without any further influence over the EPAC. Therefore, this result highlights the importance of the dynamical conditions associated with the presence of the jet, as well as the interaction with the convective forcing.

We can summarize this section by stating that the most sensitive location for EW initiation from finite-amplitude transient heating is located along the main axis of the midlevel jet around 12.5°N, 72°W. This is located over the northern part of South America and extending to the tropical EPAC trough Central America. Triggering along the midlevel jet shows an initial trough followed by a wave train over the EPAC, similar to the reference run in Fig. 4. The closer the triggering is to the jet, the bigger the response, particularly over the EPAC. If the triggering is at locations far from the midlevel jet, there is only limited EW growth. This is related to the extent to which the initial atmospheric response to the heating is collocated with the midlevel jet. These results also show that under idealized conditions, EWs over the EPAC

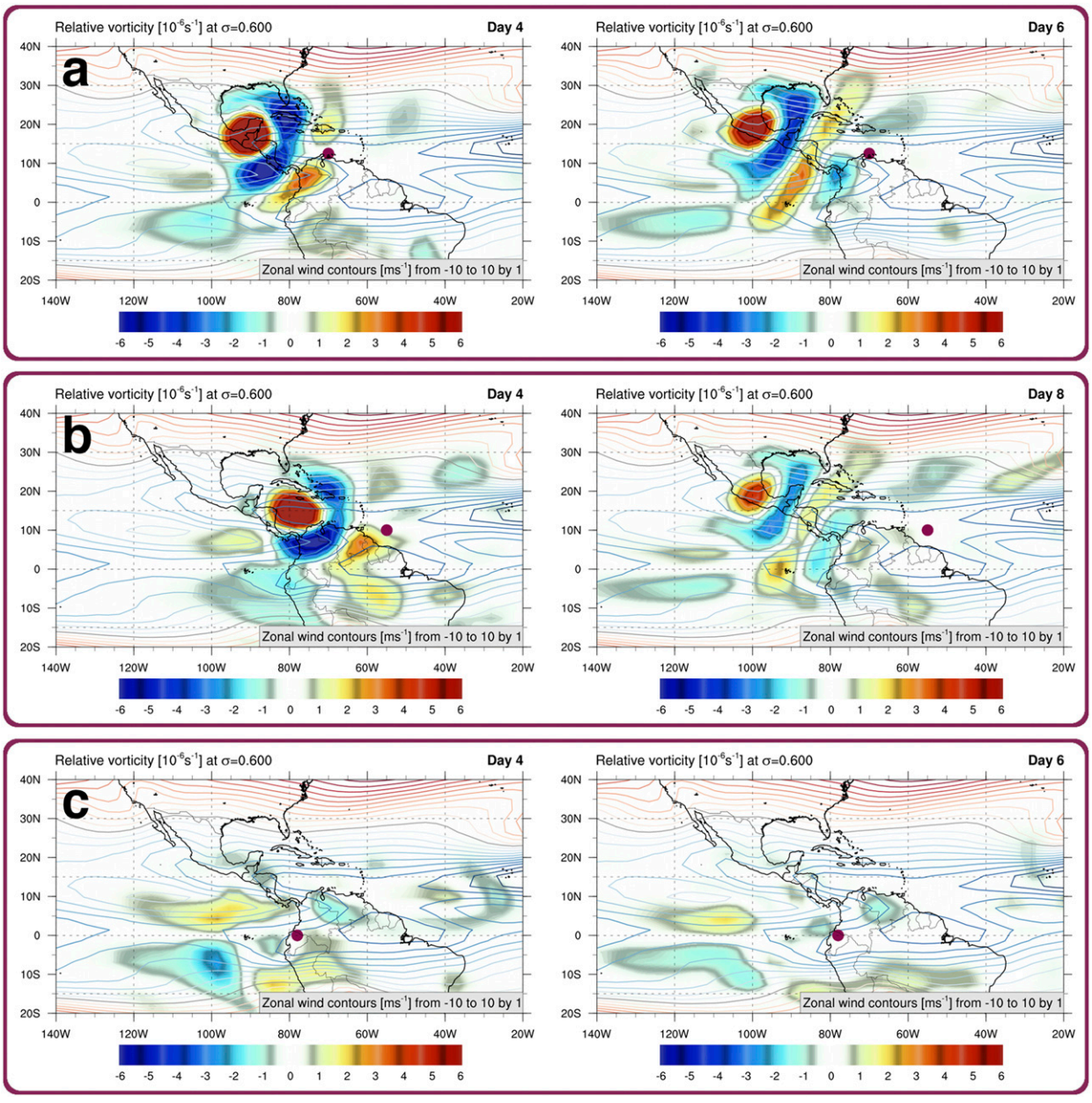

FIG. 9. Examples of relative vorticity response at $\sigma = 0.600$ (shading; $10^{-6}\,s^{-1}$) for different initial points. Heating is convective stratiform centered on (a) 12.5°N, 70°W; (b) 10°N, 55°W; and (c) 0°N, 78°W. The contours show the zonal wind ($m\,s^{-1}$) at each level, with red colors referring to westerlies and blue colors referring to easterlies.

can also be triggered by upstream heating, likely associated with AEWs.

6. Comparison of modeled easterly waves over the east Pacific and West Africa

The nature of the modeled EWs over the EPAC and West Africa are here briefly compared and contrasted. To achieve this comparison, we repeated the control experiment of Thorncroft et al. (2008) with the current model setup and compared the EWs with those from the EPAC control described above. The two simulations were both forced by the stratiform heating–cooling profile. Given that the simulated EW structures after day 1 are a dry adiabatic response to the initial heating, differences arise only due to the different environments that the EWs are evolving in. The EPAC environment differs from that over West Africa in three significant ways: (i) the midlevel easterly jet is shorter (cf. Figs. 11a,b), (ii) the PV at midlevels is stronger (0.20 PVU as compared with 0.40 PVU; 1 PVU = $10^{-6}\,K\,kg^{-1}\,m^2\,s^{-1}$), and (iii) a much

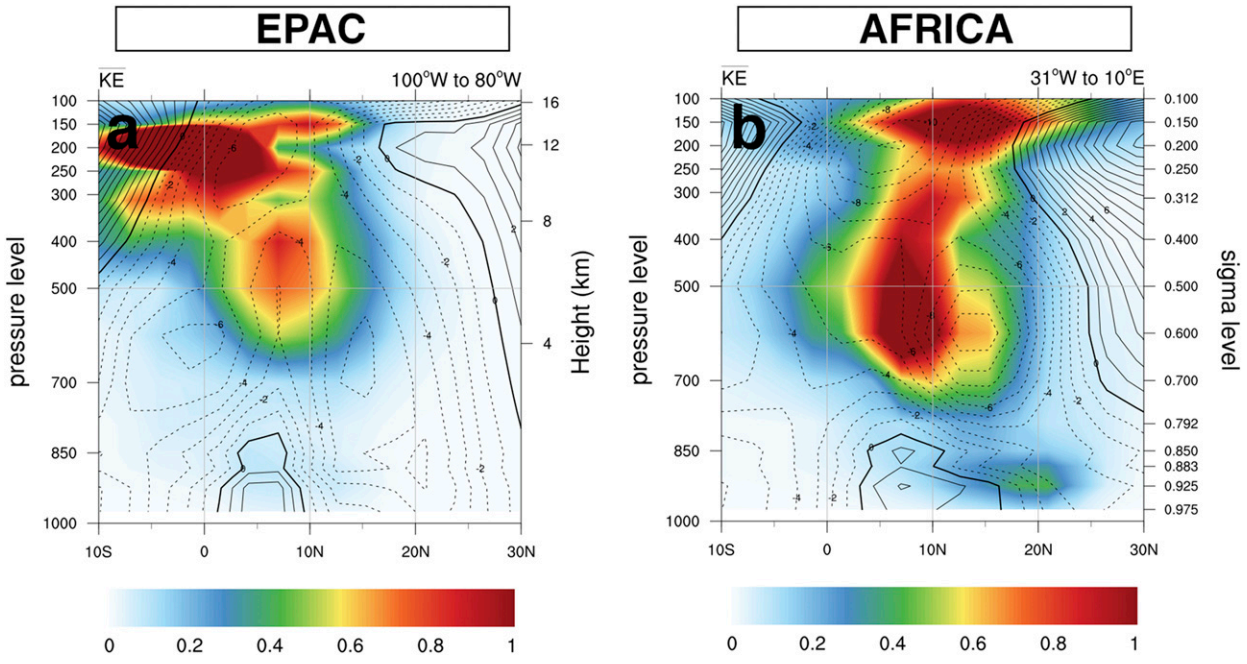

FIG. 10. Zonal-mean eddy kinetic energy (shading; $m^2 s^{-2}$) for EWs over (a) the EPAC and (b) West Africa. These are calculated from days 1 to 6 using $0.5(\overline{u'u'} + \overline{v'v'})$, where the overbar denotes a zonal mean and primes denote deviations from the zonal mean. Over the EPAC, the zonal mean is within 80°–100°W (as illustrated in Fig. 4d). The contours ($m s^{-1}$) represent the mean zonal wind within the same region. Negative contours values are dashed, and the zero contour is thickened. Over West Africa, the region considered is between 31°W and 10°E.

stronger low-level baroclinicity south of the Sahara. Given these differences, we should expect stronger EWs and more pronounced low-level amplitudes to develop over West Africa relative to those in the EPAC region.

a. Eddy kinetic energy

To explore the nature of the differences in the EWs, Fig. 10 shows a comparison of distributions of eddy kinetic energy (EKE) averaged between days 1 and 6 and zonally averaged in the two regions of EW development (EPAC: 100°–80°W; and West Africa: 31°W–10°E). Both regions exhibit a strong upper-level response close to the upper-level tropical easterly and subtropical westerly jets. Since the focus of this paper is on the EWs that develop along the midlevel jets, this upper-level response will not be discussed further but should be considered in future studies.

Both regions are characterized by an EKE maximum equatorward of their respective midlevel easterly jets. However, there are notable differences. Over the EPAC (Fig. 10a), there is a weak midlevel EKE peak, between around $\sigma = 0.600$ and $\sigma = 0.300$, with highest values above the level of the jet maximum. The evolution of the vertical structure in Figs. 5a–d highlights that the vertical structure of the midlevel EWs in the EPAC vary significantly during the first 4 days with peaks apparent at different levels. By day 4, for example, the initial EW trough has elevated amplitudes centered around $\sigma = 0.500$ but there is an additional peak in the southerlies around $\sigma = 0.300$ that may be linked to an interaction with the tropical easterly jet (not shown). Such an interaction likely also occurs over West Africa, explaining some of the upper-tropospheric amplitudes seen in Fig. 10b (see also Nicholson et al. 2007). There is also little evidence for significant low-level amplitudes, consistent with weaker low-level baroclinicity in the EPAC. In contrast, the EKE over West Africa (Fig. 10b) is stronger, with peaks located close to the level of the jet maximum and a secondary peak at low levels north of the jet, consistent with a more favorable environment for EW growth that includes the low-level baroclinicity.

b. Synoptic characteristics

Figure 11 shows the relative vorticity fields for the EWs at $\sigma = 0.600$ and $\sigma = 0.850$ for the EPAC and West African regions at days 4 and 6, respectively, when the EWs are most prominent. Clearly there are some notable differences. The EPAC waves at $\sigma = 0.600$ (Fig. 11a) have a relatively short wavelength (about 2000 km), and they are predominantly tilted NE–SW on the cyclonic shear side of the midlevel jet, with only a weak presence on the anticyclonic shear side of the jet. In contrast, the West African EWs at $\sigma = 0.600$ (Fig. 11b) have a larger wavelength (exceeding 2700 km) with significant horizontal tilts on both sides of the jet in a classic bow shape. These classic horizontal tilts for both EWs are consistent with EWs developing via barotropic growth processes. The EPAC waves at $\sigma = 0.850$ are also much weaker and less coherent than the West African waves (cf. Figs. 11c,d), consistent with Fig. 10 and the weaker EPAC baroclinicity. In addition, it should be noted that unlike AEWs, which exist for more than 10 days in the model simulation (not shown), the EPAC EWs

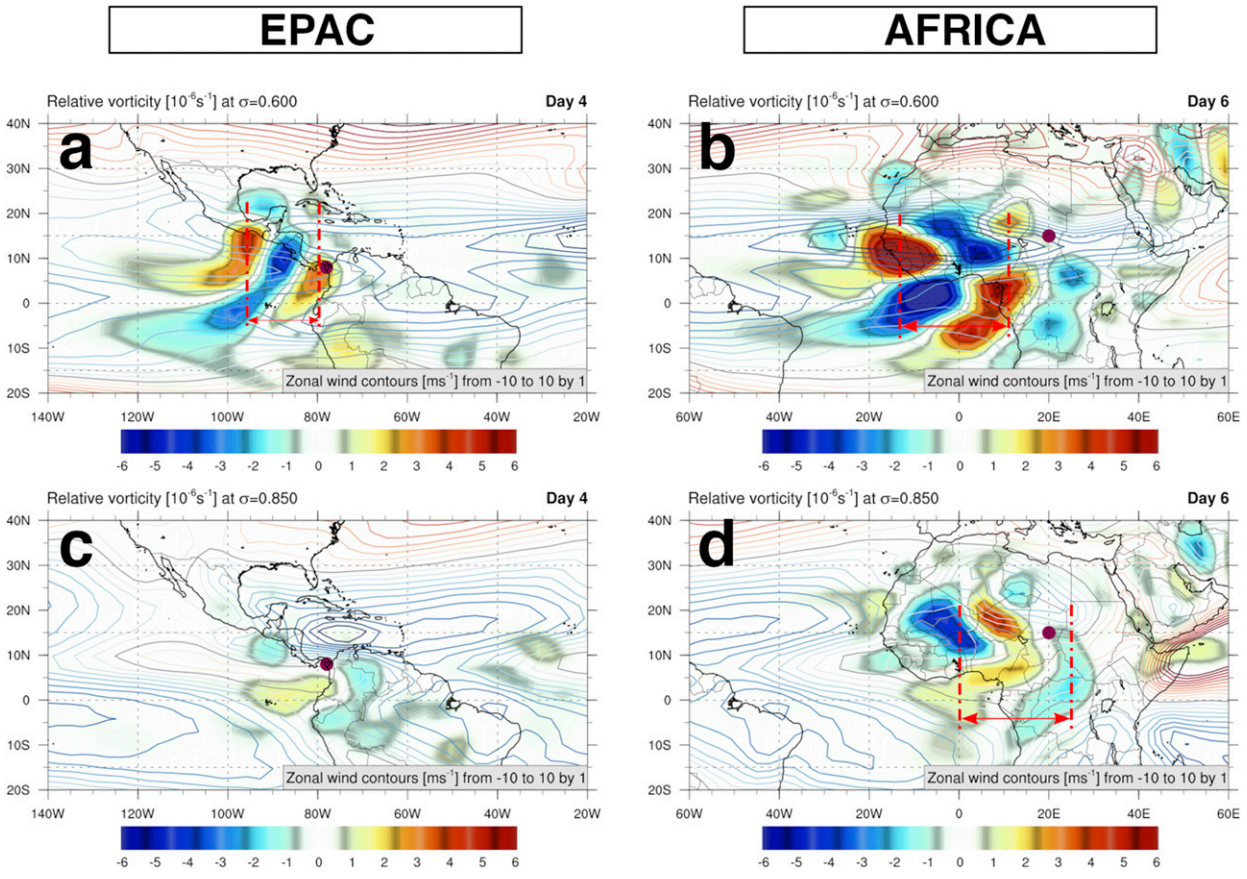

FIG. 11. Horizontal structures of EWs over (left) the EPAC and (right) West Africa at levels where covariances are close to their maximum for comparison (a),(b) at $\sigma = 0.600$ and (c),(d) at $\sigma = 0850$. The dashed red lines indicate the wavelength of the waves. The structures are retrieved from the T42L15 model setup using a stratiform convective forcing, with input from ERAI during JJAS 1980–2015.

are less long lived, dissipating soon after day 4 (see Fig. 4). This is consistent with the longer midlevel jet over Africa, already noted above.

In summary, simulated EWs over the EPAC show weaker amplitudes and shorter wavelengths when compared with those over West Africa. These differences arise due to differences in the mean state EPAC having a shorter and weaker midlevel jet with less baroclinicity.

7. Summary and discussion

The results here show that easterly waves in the EPAC region can be triggered by localized forcing (represented by finite-amplitude transient heating) in the vicinity of the midlevel jet over the EPAC–IAS region. In particular, over the Panama Bight, heating from a stratiform profile forms an initial trough that develops an EW structure in 4 days, with a wavelength and propagation speed of 2000 km and 4.6 m s^{-1}, respectively. The resulting horizontal structure and wave characteristics are in general agreement with results documented in previous studies of EWs in this region (Serra et al. 2008, 2010; Rydbeck and Maloney 2014; Rydbeck et al. 2017; Whitaker and Maloney 2020).

These results support the idea that over the EPAC, EWs can have genesis in situ (Serra et al. 2010; Rydbeck et al. 2017; Whitaker and Maloney 2020), by showing that the EWs can be triggered by upstream heating. The results suggest that in situ triggering should be considered when studying the nature and variability of EWs over the EPAC. For example, the predictability of EWs in the EPAC on synoptic time scales may be determined by the nature and predictability of upstream convection. Similarly, on longer time scales, EW activity in the EPAC may be influenced by variability in the nature and frequency of upstream convection.

In this study, latent heating is considered only as a triggering mechanism, and the interactions and feedbacks between EWs and convection (e.g., Serra et al. 2010; Janiga and Thorncroft 2016; Rydbeck and Maloney 2015) are not considered. Additionally, this idealized modeling does not include environmental characteristics such as moisture, nor model features as explicit topography, nor nonlinearities. We therefore expect amplitudes of observed individual EWs to be potentially much larger than those seen in this idealized study.

Sensitivity tests have shown that EW evolution and amplitudes are sensitive to the nature of the heating profile. The stratiform profile showed the strongest response, while the

shallow profile showed the weakest response. This is expected given the vertical gradients in the heating profiles, which drive the intensity of the initial trough (Hoskins et al. 1985), as well as its location in the vertical relative to the midlevel jet, where the EWs can take advantage of the dynamical conditions for their growth.

The most sensitive location for EW initiation is found along the midlevel jet, approximately at 12.5°N, 72°W. This region extends from the northern part of South America into the EPAC trough Central America, and it is here that dynamical conditions for instability are satisfied. EWs generated along the midlevel jet can impact continental regions during their development stage within 4–6 days (depending on location) and then potentially initiate an EW outbreak over the EPAC. At locations where dynamical conditions are not met, the transient heating does not promote the growth of EWs, as observed in an example location south of the midlevel jet.

A qualitative comparison of simulated EWs over the EPAC and West Africa showed a similar structure, but with a shorter wavelength and much weaker amplitudes over the EPAC. This is consistent with differences in the mean states for intensity and length of the midlevel jet. These differences directly impact on their development, mostly associated with barotropic growth over the EPAC, which contrasts with the barotropic–baroclinic growth over West Africa.

Future work should explore the proposed mechanism in available observations. This should include examination of anomalous convection close to the midlevel jet in the IAS region, and the extent to which this leads to downstream EWs several days later. The ability of NWP models to represent these processes should also be evaluated. Additionally, the sensitivity of the downstream response to different basic states and on the variability of the midlevel jet over the EPAC, similar to the work of Leroux et al. (2010) over West Africa, should be further explored.

Note also that it is possible that, in reality, EWs may develop along the CLLJ and subsequently move into the EPAC contributing to EW activity there. We recognize that the horizontal resolution of the model likely limits its capacity to represent the CLLJ and such developments, and so this should also be considered for future work.

Acknowledgments. We thank Yolande Serra, George Kiladis, and an anonymous reviewer for their helpful comments to improve this paper, as well as their insights into new research. Author Torres was supported by CONACYT Grant 215191 and NASA Grant NNX20AU14G.

Data availability statement. All data used in this study are publicly available. The ERA-Interim dataset (Dee et al. 2011) is accessible online (http://apps.ecmwf.int/datasets). Outgoing longwave radiation (Liebmann and Smith 1996) data are available from the National Oceanographic and Atmospheric Administration (https://psl.noaa.gov/data/gridded/data.interp_OLR.html). Rainfall data were retrieved from the National Aeronautics and Space Administration Tropical Rainfall Measurement Mission (TRMM), available at the Goddard Earth Sciences Data and Information Services Center (GES DISC) (https://disc.gsfc.nasa.gov/datasets/TRMM_3B42_7/summary/).

REFERENCES

Allison, T., H. Fuelberg, and N. Heath, 2018: Simulations of vertical water vapor transport for TC Ingrid (2013). *J. Geophys. Res. Atmos.*, **123**, 8255–8282, https://doi.org/10.1029/2018JD028334.

Amador, J. A., 1998: A climatic feature of the tropical Americas: The trade wind easterly jet. *Top. Meteor. Oceanogr.*, **5**, 91–102.

——, E. J. Alfaro, E. R. Rivera, and B. Calderón, 2010: Climatic features and their relationship with tropical cyclones over the intra-Americas seas. *Hurricanes and Climate Change*, B. J. Elsner et al., Eds., Springer, 149–173.

Belanger, J. I., M. T. Jelinek, and J. A. Curry, 2016: A climatology of easterly waves in the tropical Western Hemisphere. *Geosci. Data J.*, **3**, 40–49, https://doi.org/10.1002/gdj3.40.

Brammer, A., and C. D. Thorncroft, 2015: Variability and evolution of African easterly wave structures and their relationship with tropical cyclogenesis over the eastern Atlantic. *Mon. Wea. Rev.*, **143**, 4975–4995, https://doi.org/10.1175/MWR-D-15-0106.1.

Burpee, R. W., 1972: The origin and structure of easterly waves in the lower troposphere of North Africa. *J. Atmos. Sci.*, **29**, 77–90, https://doi.org/10.1175/1520-0469(1972)029<0077:TOASOE>2.0.CO;2.

——, 1974: Characteristics of North African easterly waves during the summers of 1968 and 1969. *J. Atmos. Sci.*, **31**, 1556–1570, https://doi.org/10.1175/1520-0469(1974)031<1556:CONAEW>2.0.CO;2.

Charney, J., and M. Stern, 1962: On the stability of internal baroclinic jets in a rotating atmosphere. *J. Atmos. Sci.*, **19**, 159–172, https://doi.org/10.1175/1520-0469(1962)019<0159:OTSOIB>2.0.CO;2.

Chelton, D. B., M. H. Freilich, and S. K. Esbensen, 2000: Satellite observations of the wind jets off the Pacific coast of Central America. Part I: Case studies and statistical characteristics. *Mon. Wea. Rev.*, **128**, 1993–2018, https://doi.org/10.1175/1520-0493(2000)128<1993:SOOTWJ>2.0.CO;2.

Cook, K. H., and E. K. Vizy, 2010: Hydrodynamics of the Caribbean low-level jet and its relationship to precipitation. *J. Climate*, **23**, 1477–1494, https://doi.org/10.1175/2009JCLI3210.1.

Crosbie, E., and Y. Serra, 2014: Intraseasonal modulation of synoptic-scale disturbances and tropical cyclone genesis in the eastern North Pacific. *J. Climate*, **27**, 5724–5745, https://doi.org/10.1175/JCLI-D-13-00399.1.

Dee, D. P., and Coauthors, 2011: The ERA-Interim reanalysis: Configuration and performance of the data assimilation system. *Quart. J. Roy. Meteor. Soc.*, **137**, 553–597, https://doi.org/10.1002/qj.828.

Diaz, M., and A. Aiyyer, 2013: The genesis of African easterly waves by upstream development. *J. Atmos. Sci.*, **70**, 3492–3512, https://doi.org/10.1175/JAS-D-12-0342.1.

Dickinson, M., and J. Molinari, 2000: Climatology of sign reversals of the meridional potential vorticity gradient over Africa and Australia. *Mon. Wea. Rev.*, **128**, 3890–3900, https://doi.org/10.1175/1520-0493(2001)129<3890:COSROT>2.0.CO;2.

Ferreira, R. N., and W. H. Schubert, 1997: Barotropic aspects of ITCZ breakdown. *J. Atmos. Sci.*, **54**, 261–285, https://doi.org/10.1175/1520-0469(1997)054<0261:BAOIB>2.0.CO;2.

Fjortoft, R., 1950: Application of integral theorems in deriving criteria of stability for laminar flows and for the baroclinic circular vortex. *Geofys. Publ.*, **17**, 1–52.

Frank, N. L., 1972: Atlantic tropical systems of 1971. *Mon. Wea. Rev.*, **100**, 268–275, https://doi.org/10.1175/1520-0493(1972)100<0268:ATSO>2.3.CO;2.

Funk, A., C. Schumacher, and J. Awaka, 2013: Analysis of rain classifications over the tropics by version 7 of the TRMM PR 2A23 algorithm. *J. Meteor. Soc. Japan*, **91**, 257–272, https://doi.org/10.2151/jmsj.2013-302.

Gordon, A. L., 1967: Circulation of the Caribbean Sea. *J. Geophys. Res.*, **72**, 6207–6223, https://doi.org/10.1029/JZ072i024p06207.

Hall, N. M. J., 2000: A simple GCM based on dry dynamics and constant forcing. *J. Atmos. Sci.*, **57**, 1557–1572, https://doi.org/10.1175/1520-0469(2000)057<1557:ASGBOD>2.0.CO;2.

——, G. N. Kiladis, and C. D. Thorncroft, 2006: Three-dimensional structure and dynamics of African easterly waves. Part II: Dynamical modes. *J. Atmos. Sci.*, **63**, 2231–2245, https://doi.org/10.1175/JAS3742.1.

——, S. Leroux, and T. Ambrizzi, 2019: Transient contributions to the forcing of the atmospheric annual cycle. *Climate Dyn.*, **52**, 6719–6733, https://doi.org/10.1007/s00382-018-4539-y.

Hertenstein, R. F. A., and W. H. Schubert, 1991: Potential vorticity anomalies associated with squall lines. *Mon. Wea. Rev.*, **119**, 1663–1672, https://doi.org/10.1175/1520-0493(1991)119<1663:PVAAWS>2.0.CO;2.

Hoskins, B. J., M. McIntyre, and A. W. Robertson, 1985: On the use and significance of isentropic potential vorticity maps. *Quart. J. Roy. Meteor. Soc.*, **111**, 877–946, https://doi.org/10.1002/qj.49711147002.

Huaman, L., and C. Schumacher, 2018: Assessing the vertical latent heating structure of the east Pacific ITCZ using the *CloudSat* CPR and TRMM PR. *J. Climate*, **31**, 2563–2577, https://doi.org/10.1175/JCLI-D-17-0590.1.

Huffman, G. J., and Coauthors, 2007: The TRMM Multisatellite Precipitation Analysis (TMPA): Quasi-global, multiyear, combined-sensor precipitation estimates at fine scales. *J. Hydrometeor.*, **8**, 38–55, https://doi.org/10.1175/JHM560.1.

Janiga, M. A., and C. D. Thorncroft, 2016: The influence of African easterly waves on convection over tropical Africa and the east Atlantic. *Mon. Wea. Rev.*, **144**, 171–192, https://doi.org/10.1175/MWR-D-14-00419.1.

Kerns, B., K. Greene, and E. Zipser, 2008: Four years of tropical ERA-40 vorticity maxima tracks. Part I: Climatology and vertical vorticity structure. *Mon. Wea. Rev.*, **136**, 4301–4319, https://doi.org/10.1175/2008MWR2390.1.

Kiladis, G. N., C. D. Thorncroft, and N. M. J. Hall, 2006: Three-dimensional structure and dynamics of African easterly waves. Part I: Observations. *J. Atmos. Sci.*, **63**, 2212–2230, https://doi.org/10.1175/JAS3741.1.

——, M. C. Wheeler, P. T. Haertel, K. H. Straub, and P. E. Roundy, 2009: Convectively coupled equatorial waves. *Rev. Geophys.*, **47**, RG2003, https://doi.org/10.1029/2008RG000266.

Leroux, S., N. M. J. Hall, and G. N. Kiladis, 2010: A climatological study of transient–mean-flow interactions over West Africa. *Quart. J. Roy. Meteor. Soc.*, **136**, 397–410, https://doi.org/10.1002/qj.474.

Liebmann, B., and C. A. Smith, 1996: Description of a complete (interpolated) outgoing longwave radiation dataset. *Bull. Amer. Meteor. Soc.*, **77**, 1275–1277, https://doi.org/10.1175/1520-0477-77.6.1274.

Maloney, E. D., and D. L. Hartmann, 2000: Modulation of eastern North Pacific hurricanes by the Madden–Julian oscillation. *J. Climate*, **13**, 1451–1460, https://doi.org/10.1175/1520-0442(2000)013<1451:MOENPH>2.0.CO;2.

Molinari, J., and D. Vollaro, 2000: Planetary- and synoptic-scale influences on eastern Pacific tropical cyclogenesis. *Mon. Wea. Rev.*, **128**, 3296–3307, https://doi.org/10.1175/1520-0493(2000)128<3296:PASSIO>2.0.CO;2.

——, D. Knight, M. Dickinson, D. Vollaro, and S. Skubis, 1997: Potential vorticity, easterly waves, and eastern Pacific tropical cyclogenesis. *Mon. Wea. Rev.*, **125**, 2699–2708, https://doi.org/10.1175/1520-0493(1997)125<2699:PVEWAE>2.0.CO;2.

——, D. Vollaro, S. Skubis, and M. Dickinson, 2000: Origins and mechanisms of eastern Pacific tropical cyclogenesis: A case study. *Mon. Wea. Rev.*, **128**, 125–139, https://doi.org/10.1175/1520-0493(2000)128<0125:OAMOEP>2.0.CO;2.

Mozer, J. B., and J. A. Zehnder, 1996: Lee vorticity production by large-scale tropical mountain ranges. Part I: Eastern North Pacific tropical cyclogenesis. *J. Atmos. Sci.*, **53**, 521–538, https://doi.org/10.1175/1520-0469(1996)053<0521:LVPBLS>2.0.CO;2.

Nicholson, S. E., A. I. Barcilon, M. Challa, and J. Baum, 2007: Wave activity on the tropical easterly jet. *J. Atmos. Sci.*, **64**, 2756–2763, https://doi.org/10.1175/JAS3946.1.

Norquist, D. C., E. E. Recker, and R. J. Reed, 1977: The energetics of African wave disturbances as observed during phase III of GATE. *Mon. Wea. Rev.*, **105**, 334–342, https://doi.org/10.1175/1520-0493(1977)105<0334:TEOAWD>2.0.CO;2.

Petersen, W. A., R. Cifelli, D. J. Boccippio, S. A. Rutledge, and C. Fairall, 2003: Convection and easterly wave structures observed in the eastern Pacific warm pool during EPIC-2001. *J. Atmos. Sci.*, **60**, 1754–1773, https://doi.org/10.1175/1520-0469(2003)060<1754:CAEWSO>2.0.CO;2.

Reed, R. J., D. C. Norquist, and E. E. Recker, 1977: The structure and properties of African wave disturbances as observed during phase III of GATE. *Mon. Wea. Rev.*, **105**, 317–333, https://doi.org/10.1175/1520-0493(1977)105<0317:TSAPOA>2.0.CO;2.

Romero-Centeno, R., J. Zavala-Hidalgo, and G. B. Raga, 2007: Midsummer gap winds and low-level circulation over the eastern tropical Pacific. *J. Climate*, **20**, 3768–3784, https://doi.org/10.1175/JCLI4220.1.

Rydbeck, A. V., and E. D. Maloney, 2014: Energetics of east Pacific easterly waves during intraseasonal events. *J. Climate*, **27**, 7603–7621, https://doi.org/10.1175/JCLI-D-14-00211.1.

——, and ——, 2015: On the convective coupling and moisture organization of east Pacific easterly waves. *J. Atmos. Sci.*, **72**, 3850–3870, https://doi.org/10.1175/JAS-D-15-0056.1.

——, ——, and G. J. Alaka Jr., 2017: In situ initiation of east Pacific easterly waves in a regional model. *J. Atmos. Sci.*, **74**, 333–351, https://doi.org/10.1175/JAS-D-16-0124.1.

Schumacher, C., R. A. Houze Jr., and I. Kraucunas, 2004: The tropical dynamical response to latent heating estimates derived from the TRMM Precipitation Radar. *J. Atmos. Sci.*, **61**, 1341–1358, https://doi.org/10.1175/1520-0469(2004)061<1341:TTDRTL>2.0.CO;2.

Serra, Y. L., and R. A. Houze Jr., 2002: Observations of variability on synoptic timescales in the east Pacific ITCZ. *J. Atmos. Sci.*, **59**, 1723–1743, https://doi.org/10.1175/1520-0469(2002)059<1723:OOVOST>2.0.CO;2.

——, G. N. Kiladis, and M. F. Cronin, 2008: Horizontal and vertical structure of easterly waves in the Pacific ITCZ. *J. Atmos. Sci.*, **65**, 1266–1284, https://doi.org/10.1175/2007JAS2341.1.

——, ——, and K. I. Hodges, 2010: Tracking and mean structure of easterly waves over the intra-Americas sea. *J. Climate*, **23**, 4823–4840, https://doi.org/10.1175/2010JCLI3223.1.

Tai, K.-S., and Y. Ogura, 1987: An observational study of easterly waves over the eastern Pacific in the northern summer using FGGE data. *J. Atmos. Sci.*, **44**, 339–361, https://doi.org/10.1175/1520-0469(1987)044<0339:AOSOEW>2.0.CO;2.

Takayabu, Y. N., and T. Nitta, 1993: 3-5 day-period disturbances coupled with convection over the tropical Pacific Ocean. *J. Meteor. Soc. Japan*, **71**, 221–246, https://doi.org/10.2151/jmsj1965.71.2_221.

Thorncroft, C. D., and B. Hoskins, 1994: An idealized study of African easterly waves. I: A linear view. *Quart. J. Roy. Meteor. Soc.*, **120**, 953–982, https://doi.org/10.1002/qj.49712051809.

——, N. M. Hall, and G. N. Kiladis, 2008: Three-dimensional structure and dynamics of African easterly waves. Part III: Genesis. *J. Atmos. Sci.*, **65**, 3596–3607, https://doi.org/10.1175/2008JAS2575.1.

Toma, V. E., and P. J. Webster, 2010a: Oscillations of the intertropical convergence zone and the genesis of easterly waves. Part I: Diagnostics and theory. *Climate Dyn.*, **34**, 587–604, https://doi.org/10.1007/s00382-009-0584-x.

——, and ——, 2010b: Oscillations of the intertropical convergence zone and the genesis of easterly waves. Part II: Numerical verification. *Climate Dyn.*, **34**, 605–613, https://doi.org/10.1007/s00382-009-0585-9.

Whitaker, J. W., and E. D. Maloney, 2020: Genesis of an east Pacific easterly wave from a Panama Bight MCS: A case study analysis from June 2012. *J. Atmos. Sci.*, **77**, 3567–3584, https://doi.org/10.1175/JAS-D-20-0032.1.

Zipser, E. J., D. J. Cecil, C. Liu, S. W. Nesbitt, and D. P. Yorty, 2006: Where are the most intense thunderstorms on Earth? *Bull. Amer. Meteor. Soc.*, **87**, 1057–1072, https://doi.org/10.1175/BAMS-87-8-1057.

Zuluaga, M. D., and R. A. Houze, 2015: Extreme convection of the near-equatorial Americas, Africa, and adjoining oceans as seen by TRMM. *Mon. Wea. Rev.*, **143**, 298–316, https://doi.org/10.1175/MWR-D-14-00109.1.